MATERIALS CHEMISTRY FRONTIERS

RESEARCH ARTICLE

View Article Online
View Journal | View Issue



Cite this: *Mater. Chem. Front.*, 2025, **9**, 3572

# Raising the operating temperature of layered perovskite phase-change materials beyond 100 °C *via* alkylammonium extension

Alba Prats, †[a] Laura Ribas-Cabello,†[b] Clàudia Pérez-Junyent,[a] Xavier Carpena,[c] Roeland Boer,[c] Guillaume F. Nataf,[d] Fabien Giovanelli,[d] Gerardo Carrasco,[ab] María Barrio,[a] Josep Lluís Tamarit,[a] Pol Lloveras *[a] and Roc Matheu *[b]

Two-dimensional halide perovskites hold promise for thermal energy storage and barocaloric cooling and heating. The rich chemical flexibility of halide perovskites containing alkylammonium cations has not yet been fully scanned, especially for medium-temperature operations (80–150 °C). This temperature range is generating interest in the industry sector, where waste heat recovery and sustainable heat pumping are in high demand. Here, we expand the operational temperature of this material class by synthesizing two-dimensional halide perovskites with an increased number of carbons ($n$) in the alkylammonium cations ($C_nH_{2n+1}NH_3$) up to $n$ = 22. We find that the previously unreported perovskites, $(C_nH_{2n+1}NH_3)_2CuX_4$ (X = Cl, Br; $n$ = 18–22, even), display phase transitions in the 90–110 °C range, exceeding those of the related compounds by 20–30 °C. Furthermore, bromide and chloride compounds display unexpected differences in their structural and thermodynamic features. Depending on the halide, single-crystal X-ray structures reveal different conformations in the carbon atoms closest to the ammonia group and tilting angles of the organic cations with respect to the inorganic sublattice, resulting in denser packing for the bromide derivatives. Also, the bromide perovskites display a main phase transition with significant latent heat, whereas the chloride perovskites exhibit a sequence of less energetic transitions. The phase transitions in the 90–110 °C range, low hysteresis (0.1–1 °C), and high-pressure sensitivity of the transition ($dT/dp$ ~ 300 °C GPa$^{-1}$) render them interesting candidates for both barocaloric and thermal energy storage applications at medium temperatures.

Received 30th September 2025,
Accepted 10th November 2025

DOI: 10.1039/d5qm00712g

rsc.li/frontiers-materials



## 1. Introduction

Phase-change materials (PCMs) exhibit energetic first-order phase transitions (FOPTs) that can be functionalized for thermal management applications.[1,2] There is growing interest in medium-temperature ranges (80–200 °C), where PCMs could offer significant opportunities to advance decarbonization and sustainability in numerous industries (*e.g.*, textile, food and beverage, and pulp and paper).[3] On the one hand, industrial waste heat is estimated to account for 6–15% of overall energy consumption, with a significant portion being low-grade (<200 °C).[4,5] Here, PCMs can enhance thermal inertia and process efficiency as thermal energy storage media by recovering and reusing waste heat. On the other hand, PCMs can leverage pressure-driven caloric effects for heat pumping to replace fuel burners and hydrofluorocarbon fluids in heating processes.[6] For both applications, solid–solid PCMs offer mechanically stable, leakage-free, shapeable, and easy-handling media compared to fluid PCMs.[7–9]

Among solid–solid PCMs, two-dimensional (2D) perovskites containing alkylammonium cations were identified early in the 1980s for thermal energy storage[10] due to one or a sequence of FOPTs with overall latent heats exceeding 50 J g$^{-1}$. Recently, they have been proposed as solid refrigerants[14] because the FOPTs can also be driven by pressure (Fig. 1a).[14] With the $A_2BX_4$ formula, the structure of 2D perovskites comprises a layer of corner-sharing $BX_6$ octahedra (*e.g.*, B–X = Cu–Cl, Cu–Br, Mn–Cl, Cd–Cl, Hg–Cl, Pb–Cl), separated by a bilayer of organic cations,

[a] *Department of Physics, EEBE, and Barcelona Research Center in Multiscale Science and Engineering, Universitat Politècnica de Catalunya, Avinguda Eduard Maristany 10–14, 08019 Barcelona, Catalunya, Spain. E-mail: pol.lloveras@upc.edu*
[b] *Departament de Química Inorgànica i Orgànica, Institut de Química Teòrica i Computacional, Universitat de Barcelona, Carrer Martí i Franquès 1–11, Barcelona, 08028, Catalunya, Spain. E-mail: roc.matheu@ub.edu*
[c] *BL13-XALOC, ALBA Synchrotron (CELLS), Carrer de la Llum 2–26, Cerdanyola del Vallès, Catalunya, Spain*
[d] *GREMAN UMR7347, CNRS, University of Tours, Rue de la Chocolaterie, 41029, Blois, France*
† These authors contributed equally.

 

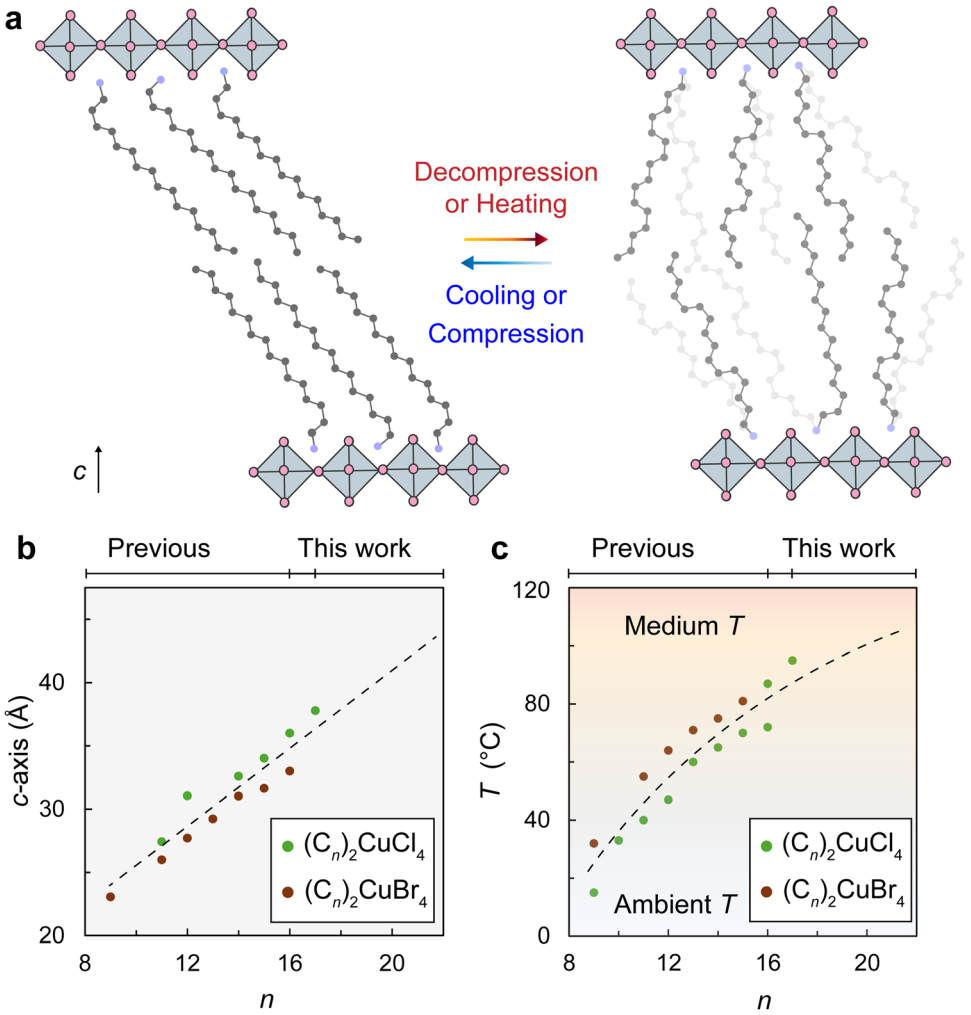


Fig. 1 (a) Schematic illustration of the low-temperature and high-temperature phases in a solid–solid phase transition for $(C_n)_2CuX_4$ (X = Cl, Br). (b) Variation of the *c*-axis in the low temperature phase and (c) temperature of the most energetic phase transitions ($\Delta H > 20$ J g$^{-1}$) of a series of $(C_n)_2CuX_4$ (X = Cl, Br) with an increasing number of carbon atoms (*n*) in the alkylammonium cations ($C_n^+$). Previous data extracted from ref. 10–13. Fig. S17 displays the data reported in this work for $(C_n)_2CuX_4$ (X = Cl, Br) with *n* = even 16–22.

such as alkylammonium cations ($C_nH_{2n+1}NH_3^+$, $C_n^+$ for short) (Fig. 1a and b).[15–22] Most known alkylammonium perovskites display transition temperatures below 90 °C (Fig. 1c) due to the previous focus on near-ambient temperature applications.[23] The FOPT temperatures increase with the number of carbon atoms (*n*) of $C_n^+$ (Fig. 1c), similar to the melting temperatures of *n*-alkanes.[24] To our knowledge, the highest temperatures have been achieved for $(C_n)_2CuX_4$ (X = Cl, Br) with *n* = 16–17 (Fig. 1c).[10–13] In this work, we aimed to develop novel halide perovskites that display large latent heat above >80 °C for medium-temperature thermal management applications. Herein, we report on the synthesis and characterization of $(C_n)_2CuX_4$ with an increasing number of carbons (*n* = 16, 18, 20, and 22)—which remained unexplored—and we show that they display operation temperatures between 80 and 110 °C. We also report on the single-crystal X-ray diffraction structures for $(C_{16})_2CuX_4$ (X = Cl, Br), $(C_{18})_2CuCl_4$, and $(C_{22})_2CuBr_4$, which reveal that the halide has a significant effect on the packing of the organic layer. Whereas bromide perovskites show a single major FOPT with large latent heat, chloride perovskites increase the number of FOPT with smaller latent heats. Thus, the nature of the halide critically impacts the transition thermodynamics due to differences in the packing of the organic sublattice. Finally, we also determine their temperature-pressure phase diagrams. The increased transition temperature, low hysteresis (0.1–1 °C), and high d*T*/d*p* (300 °C GPa$^{-1}$) suggest these materials as promising solid-state PCMs candidates for thermal energy storage and pressure-driven heat pumping at a temperature range (90–110 °C) relevant for many industries.

## 2. Results and discussion

### 2.1. Synthesis and structure of $(C_nH_{2n+1}NH_3)_2CuX_4$

We prepared $(C_nH_{2n+1}NH_3)_2CuX_4$ (X = Cl, Br), containing an increasing length of $C_n^+$ (*n* = even 16–22), by combining $CuX_2$

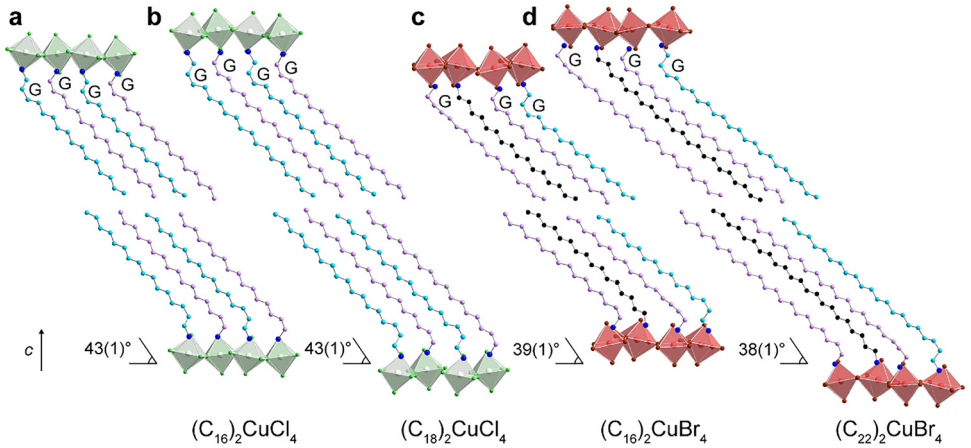


Fig. 2 Single-crystal X-ray diffraction (SCXRD) structures for (a) $(C_{16})_2CuCl_4$, (b) $(C_{18})_2CuCl_4$, (c) $(C_{16})_2CuBr_4$, and (d) $(C_{22})_2CuBr_4$. Green and red octahedra represent $CuCl_6$ and $CuBr_6$, respectively. Dark blue spheres represent N atoms. The $(C_n)_2CuX_4$ (X = Cl, Br) perovskites contain one chain with *gauche* (*G*) conformation in the C1–C2 bond (pink; torsion angle for G conformation = 72° for $C_{16}^+$ and 79° for $C_{18}^+$) and one chain with a G conformation in the C2–C3 bond (turquoise; torsion angle = 79° for $C_{16}^+$, and 69° for $C_{18}^+$). The bromide perovskite contains two chains with G conformation in the C1–C2 bond (pink; torsion angle = 68° and 84° for $C_{16}^+$, and 67° and 84° for $C_{22}^+$), a chain with G conformation in the C2–C3 bond (turquoise; torsion angle = 67° for $C_{16}^+$ and 60° for $C_{22}^+$), and a chain without G conformation bonds (black). Tilt angles between $C_n^+$ and the *ab*-plane are indicated in each case.

and $C_nX$ ethanol solutions and filtering the yellow (X = Cl) and purple powders (X = Br). We also obtained crystals suitable for single-crystal X-ray diffraction (SCXRD) for $(C_n)_2CuCl_4$ ($n$ = 16 and $n$ = 18) and $(C_n)_2CuBr_4$ ($n$ = 16 and 22) (Fig. 2 and Tables S1–S4). At −173 °C, the SCXRD structures display the typical 2D perovskite lattice,[16,18,19] in which a bilayer of $C_n^+$ cations separates the plane formed by corner-sharing Cu–X octahedra (Fig. 2). The same structure is expected at ambient temperature due to the absence of phase transitions between the two temperatures. We measured powder X-ray diffraction (PXRD) on $(C_n)_2CuX_4$, indexing the crystallographic planes based on the SCXRD data and, thus, confirming the nature and purity of all powders (Fig. 3 and Fig. S1–S4). Elemental analysis further confirmed the purity of all perovskites, and thermal gravimetric analysis indicates that the perovskites are thermally stable up to 205 °C ($(C_n)_2CuCl_4$) and 175 °C ($(C_n)_2CuBr_4$) (Fig. S13 and S14).

The combined PXRD and SCXRD data reveal some of the effects of the halide and the alkylammonium in the ordered $(C_n)_2CuX_4$ structures. The PXRD peaks corresponding to the (00$l$) planes ($l$ = 1, 2, 3) appear at smaller angles with an increasing number of carbons ($n$), indicating an expansion in the interplanar *c*-axis (Fig. 3). As observed for most 2D perovskites,[25] the inorganic plane formed by Cu–X octahedra is larger for the bromide perovskite (~59 Å$^2$) than for the

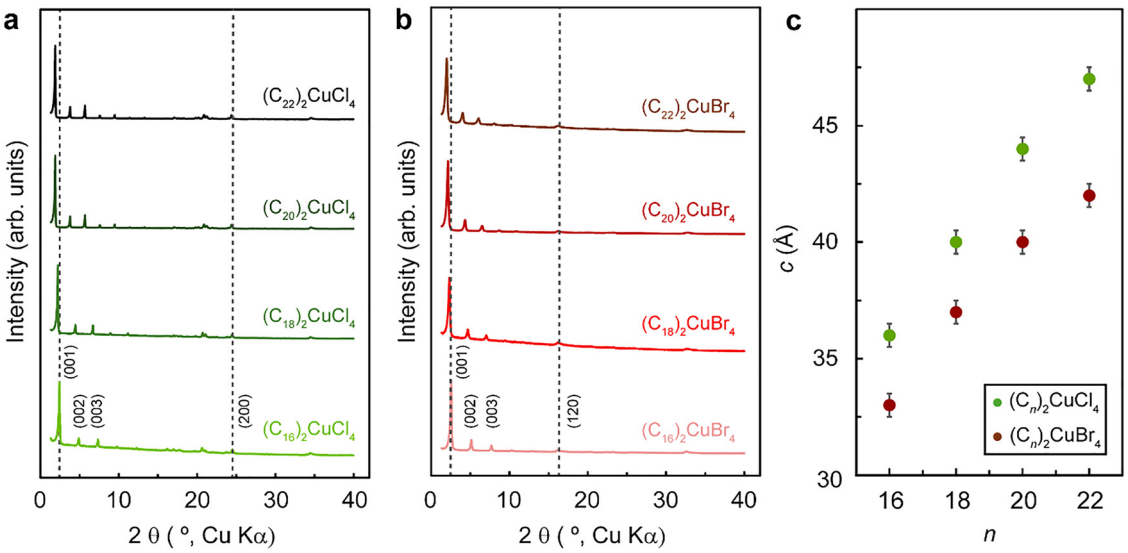


Fig. 3 Powder X-ray diffraction (PXRD) patterns for (a) $(C_n)_2CuCl_4$ and (b) $(C_n)_2CuBr_4$ ($n$ = 16, 18, 20, 22). (c) *c*-axis as a function of the number of carbons in $C_n^+$. The calculated *c*-axis parameters were calculated assuming an orthorhombic cell. The error was estimated by comparing the calculated *c*-axis value to that of the $(C_{16})_2CuCl_4$, $(C_{18})_2CuCl_4$, $(C_{16})_2CuBr_4$, and $(C_{22})_2CuBr_4$ SCXRD structures.

chloride perovskite (~54 Å$^2$) owing to longer Cu–Br bonds. However, the increased Cu–Br bonds do not lead to longer *c*-axes for $(C_n)_2CuBr_4$. For example, the *c*-axis is 33.3 Å for $(C_{16})_2CuBr_4$ and 36.0 Å for $(C_{16})_2CuCl_4$ (Fig. 3c and Table S5). The smaller *c*-axis for bromide perovskites arises from a smaller tilt angle between the Cu–X inorganic plane and the chains (Fig. 2). In halide perovskites[26] and related compounds,[27] decreased angle tilts occur in compounds based on larger halides (*e.g.*, Br) to maximize van der Waals interactions between the organic chain and the inorganic plane.

Another structural difference in $(C_n)_2CuX_4$ (X = Cl, Br) is the conformation of the C–C bonds close to the inorganic plane. Changes in this conformation are known to vary the unit-cell volume of both low- and high-temperature phases.[14] Thus, they are involved in the volume changes in solid–solid phase transformations of layered perovskites. For $(C_n)_2CuCl_4$, the $C_n^+$ chains in the bilayer adopt two different conformations. One chain displays a *gauche* conformation (G) in the C1–C2 bond (pink chain, Fig. 2a and b), and the other shows a G conformation in the C2–C3 bond (turquoise chain, Fig. 2a and b). Interestingly, the bromide perovskite comprises the same two chains (Fig. 2c and d) and another without a G conformation bond (black chain, Fig. 2c and d) owing to a doubled *b*-axis (Fig. S7). The chloride perovskites are consistent with most reported 2D halide perovskite structures based on Cu–Cl.[11,28–31] Contrastingly, the SCXRD structures for $(C_{16})_2CuBr_4$ and $(C_{22})_2CuBr_4$ differ from previously reported Cu–Br perovskite structures.[32,33] The shorter $C_n^+$ in Cu–Br structures ($n$ = 4, 9) is probably responsible for a distinct packing of the organic layer.

We restricted our study to new $(C_n)_2CuX_4$ with $C_n^+$ containing even $n$ (18–22) due to the limited commercial availability of alkylamines with odd $n$ (21) and $n > 22$. For completeness, we also prepared $(C_{19})_2CuX_4$ (X = Cl, Br) following the same synthetic protocols and characterized the powders by PXRD (Fig. S5). Finally, we also explored the possibility of developing solvent-free synthetic methods based on mechanochemistry, which is increasingly used in other applications involving halide perovskites.[34] By ball-milling stoichiometric amounts of $CuBr_2$ and $(C_{16})Br$ with inert $ZrO_2$ balls, we obtained $(C_{16})_2CuBr_4$. PXRD measurements confirmed the nature and purity of the solvent-free prepared perovskite (Fig. S6).

### 2.2. Thermodynamic characterization of phase transitions at normal pressure

We conducted differential scanning calorimetry (DSC) for $(C_n)_2CuX_4$ (X = Cl, Br, $n$ = even 16–22), including the $(C_{16})_2CuBr_4$ sample prepared by ball milling (Fig. 4 and Fig. S8). The endothermic transition temperatures were determined from the peak onsets (Fig. 4a and b), and the latent heats ($\Delta H$) were calculated from peak integrations after baseline subtraction (indicated by the area of the circles in Fig. 4c). DSC curves display peaks associated with FOPTs, revealing a strong dependence of the polymorphism on the halide (Fig. 4a and b). The bromide perovskites show a main FOPT with a large latent heat that increases with $n$ ($\Delta H \sim 57$ J g$^{-1}$, $n$ = 16; $\Delta H \sim 67$ J g$^{-1}$, $n$ = 22), most likely associated with the chain melting.[35] Additionally, one or two small FOPT peaks ($\Delta H \sim 0.5$–7 J g$^{-1}$), likely related to chain rotation around its axis, appear quite far in temperature. The $\Delta H$ for $(C_{16})_2CuBr_4$—this work's only previously reported bromide perovskite—coincides with the literature.[11] Overall, the DSC of the $(C_{16})_2CuBr_4$ sample synthesized *via* ball milling coincides with that of the sample prepared in solution (Fig. S8). However, a significantly lower latent heat for the main transition is observed in the ball-milled

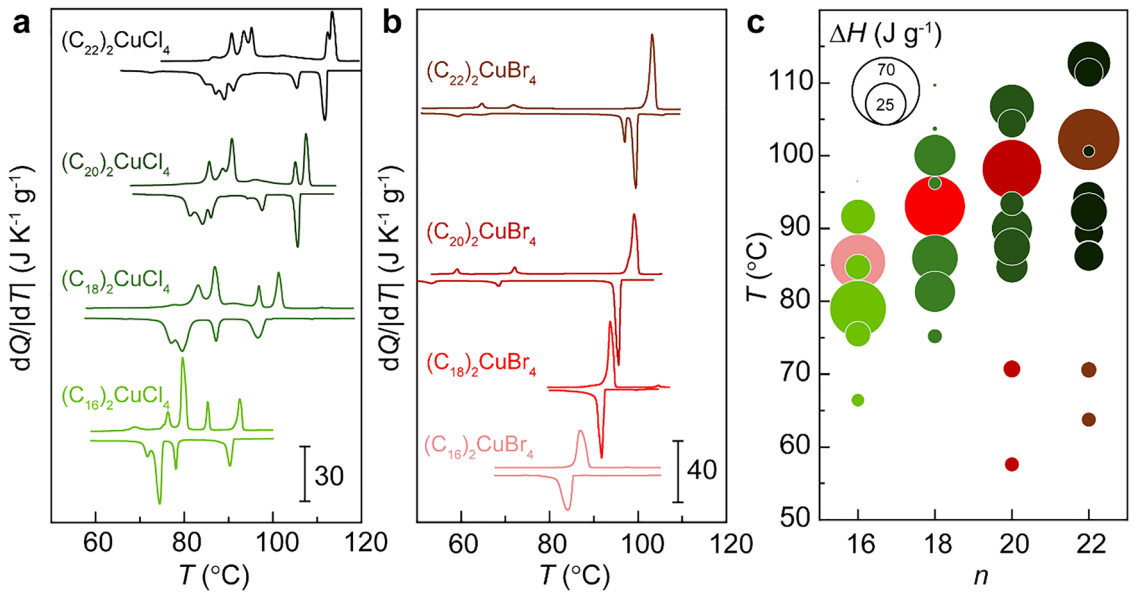


Fig. 4 Differential scanning calorimetry (DSC) at 2 °C min$^{-1}$ for (a) $(C_n)_2CuCl_4$ and (b) $(C_n)_2CuBr_4$ ($n$ = even 16–22). (c) Endothermic transition temperatures for $(C_n)_2CuX_4$ (X = Cl, greenish; X = Br, redish) as a function of the number of carbon atoms ($n$) in $C_n^+$. The circle areas are proportional to the transition latent heat, as the legend shows.

sample ($\Delta H \sim 47$ J g$^{-1}$) compared to the solution synthesis ($\Delta H \sim 57$ J g$^{-1}$). The difference in crystallite size between the solution-prepared samples ($\sim$10 μm) and ball-milled samples ($\sim$100 nm)[34] is likely to result in a higher occurrence of surface defects for the smallest crystallites.[34] Thus, we attribute the latent heat differences to inhomogeneities, strain, or defects in the ball-milling synthesis sample.[34]

The chloride perovskites display much richer polymorphism, featuring 4–6 phase transitions of comparable latent heats ($\Delta H \sim 15$–$40$ J g$^{-1}$) within a narrow temperature interval (30 °C). These results suggest that the chain disorder in $(C_n)_2CuCl_4$ occurs at different steps, with likely one or two different $C_n^+$ conformations arising across each FOPT. Phase dynamics, however, is beyond the scope of this work and would require rigorous spectroscopic investigations. The combined FOPTs in $(C_n)_2CuCl_4$ compounds sum up a larger $\Delta H$ than those in $(C_n)_2CuBr_4$ compounds and increase slightly when increasing $n$, both per unit mass and mole (Fig. S9). Our results for $(C_{16})_2CuCl_4$ also agree with the literature, although the two lower-temperature transitions were previously considered conjointly.[36]

The transition temperatures of the chloride and bromide perovskites increase with increasing $n$, reaching 110 °C for $(C_{22})_2CuCl_4$ and 101 °C for $(C_{22})_2CuBr_4$. The transition temperature rate with respect to $n$ is comparable for all transitions. However, a slower rate is observed for longer cations ($\Delta T \sim 8$ °C for $n = 16 \rightarrow 18$, $\Delta T \sim 5$ °C for $n = 20 \rightarrow 22$). This is consistent with a slower growth rate at larger $n$ also exhibited by $c$ length (Fig. 3c) and the latent heat on average (Fig. 4c and Fig. S9, Table S6). The length variation is smaller at larger $n$, resulting in a smaller rate. The same trend has been observed for perovskites with $n < 16$ (Fig. 1c).[10,11] For most FOPTs, the slight difference between endothermic and exothermic transition temperatures indicates a very low hysteresis, especially in the bromide perovskites ($\Delta T_{hys} \sim 0.1$–$1$ °C), which is an overall trend shown by alkylammonium perovskites.[14,32] This is a remarkable advantage for thermal management applications due to the reduced energy losses. The low hysteresis compares favorably with other colossal latent heat materials, such as organic plastic crystals, which show hysteresis typically above 10 °C.[37] Notably, the $(C_{22})_2CuBr_4$ hysteresis allows distinguishing between two different FOPTs on cooling that appear jointly on heating (Fig. 4b).

### 2.3. Thermodynamic characterization of phase transitions at high pressure

We performed high-pressure differential thermal analysis measurements to construct temperature-pressure phase diagrams (Fig. 5) and to assess their potential as barocaloric materials at medium temperatures. With increasing pressure, the endothermic and exothermic transition peaks for $(C_n)_2CuX_4$ (X = Cl, Br, $n$ = even 16–22) shift to higher temperatures (Fig. 5 and Fig. S9–S11). For some of the perovskites, a peak splits above a given pressure (*e.g.*, phase IV in $(C_{18})_2CuBr_4$, Fig. 5f), indicating the presence of a new high-pressure phase and a triple point.[14] The coordinates for the triple points can be found in Table S7. This behavior suggests that changes in disorder arising across a single transition below the triple point (*e.g.*,

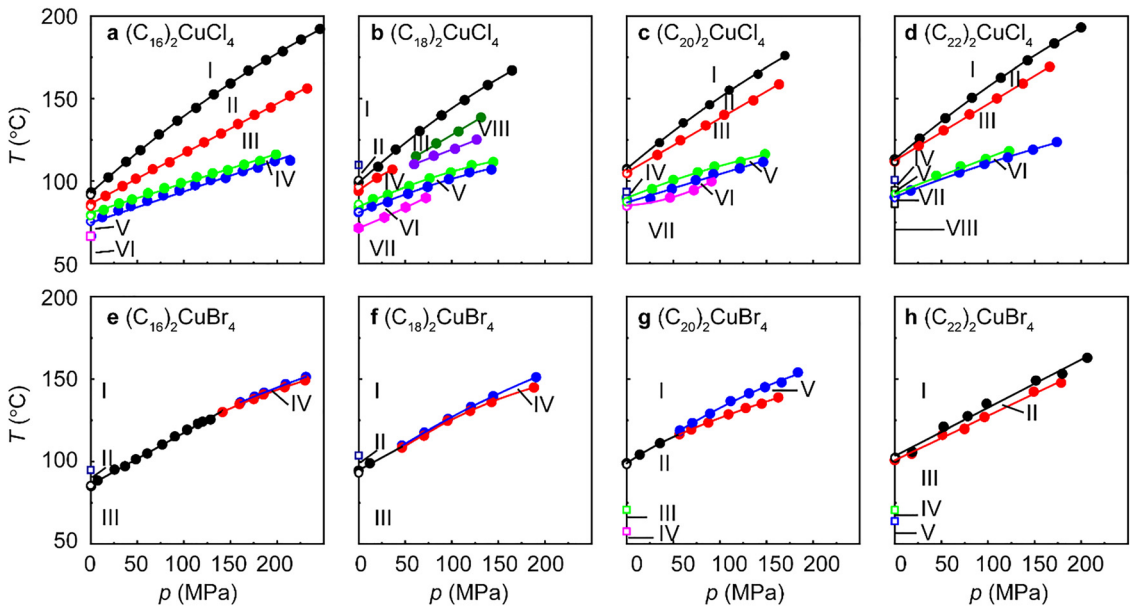


Fig. 5 Temperature-pressure phase diagrams for (a)–(d) $(C_n)_2CuCl_4$ and (e)–(h) $(C_n)_2CuBr_4$ ($n$ = even 16–22). The transition temperatures were determined from the peak onsets, which allowed us to construct the equilibrium phase diagrams using the endothermic transition data. Phase labels are ordered from high to low temperatures and from atmospheric to high pressures. Empty circles correspond to DSC data in agreement with high-pressure calorimetry data, which are plotted as solid circles. Empty squares correspond to DSC data that were not detected using high-pressure calorimetry. The lower sensitivity of the high-pressure calorimeter did not allow for unambiguous measurement of the less energetic peaks detected using conventional DSC, especially the $(C_n)_2CuBr_4$ transitions between 40 and 80 °C.

 

emergence of different conformations, chain rotations) could occur in two steps above it. Therefore, thermomechanical conditions are likely to affect the disorder of $C_n^+$ in the various phases. At all triple points, the number of phases increases with growing pressure (*i.e.*, pressure favors enantiotropy). The temperature range of stability of these high-pressure phases remains narrow due to the similar values for d$T$/d$p$ for the two transitions involved. For most materials and all energetic transitions, the higher the transition temperature (at a given pressure), the larger the transition shift d$T$/d$p$, which anticipates triple points at (theoretically) negative pressure. Therefore, as pressure enhances the stability of more phases, Cl atoms seem to exert higher chemical pressure than Br atoms.[38–42]

The calculated d$T$/d$p$ for $(C_n)_2CuX_4$ (X = Cl, Br, $n$ = even 16–22) are, overall, very significant ($\sim$300 K GPa$^{-1}$), and most of them decrease slightly with the applied pressure due to the convexity of the coexistence lines (Table S6). Overall, transition hysteresis slightly increases with increasing pressure because exothermic transitions exhibit lower d$T$/d$p$ than endothermic ones (Fig. S10 and S11). However, hysteresis remains low for most transitions (including the most energetic). Altogether, large values for $\Delta H$ and d$T$/d$p$ and low hysteresis suggest the possibility of harvesting colossal reversible barocaloric effects under low pressures in the medium temperature range[37] and their use in barocaloric thermal batteries.[43,44] Using the Clausius–Clapeyron equation at atmospheric pressure, we calculated transition volume changes on heating (Table S6), obtaining $\Delta V/V$ $\sim$6% for $(C_n)_2CuBr_4$ and $\sim$3% for $(C_n)_2CuCl_4$. These values are large and might challenge mechanical stability, yet they are smaller than typical volume changes at melting points in solid–liquid PCMs,[37] thus facilitating device design.

The polymorphic behavior observed for $(C_n)_2CuCl_4$ is reminiscent of that in $n$-alkanes ($CH_3$–$(CH_2)_{n-2}$–$CH_3$).[24] On heating from the fully ordered crystal phase up to the melting, $n$-alkanes display a series of intermediate phases exhibiting rotations around the chain axis, similar to the dynamic disorder reported for $(C_n)_2BX_4$.[14,32] The melting temperatures of $n$-alkanes increase gradually with $n$ in a magnitude comparable to major solid–solid transitions in 2D hybrid perovskites. In particular, the dependence of the transition temperature on $n$ around $n$ = 18 is d$T$/d$n$ $\sim$ 4.6 K for $n$-alkanes and d$T$/d$n$ $\sim$ 3.2 K for $(C_n)_2CuBr_4$ and d$T$/d$n$ $\sim$ 3.2 K for $(C_n)_2CuCl_4$.[45] In contrast to $n$-alkanes, the inorganic sublattice in $(C_n)_2BX_4$ provides a crystalline framework for the disordered $C_n^+$. Consequently, the organic molecules do not acquire translational freedom as naturally occurring in molten $n$-alkanes. Instead, the disorder in the hybrid perovskites consists of the emergence and mobility along the chain of different $C_n^+$ conformations,[35] resulting in solid–solid transitions. PCMs displaying solid–solid transitions are highly beneficial for thermal management applications because they avoid leakage issues and display low vapor pressures, representing a potential advantage over solid–liquid PCMs. The low vapor pressure of $(C_n)_2CuX_4$ (X = Cl, Br, $n$ = even 16–22) was confirmed by thermal gravimetric analysis (Fig. S13 and S14). Like in $n$-alkanes,[45] two-dimensional halide perovskites show odd–even effects arising from the packing of the organic sublattices.[46] Because we restricted our findings to perovskites containing alkylammonium with an even $n$, the trends observed in $(C_n)_2CuX_4$ (X = Cl, Br, $n$ = even, 16–22) may not be extrapolated to perovskites containing an odd $n$ (*e.g.*, 21, 23).

Despite the large values for $\Delta H$ exhibited by our compounds, their energy densities are still lower than those of organic plastic crystals in a comparable temperature range (*e.g.*, pentaglycerine, 166 J g$^{-1}$ at 80 °C).[47] Nevertheless, organic plastic crystals exhibit larger vapor pressures, which is detrimental to thermal stability and challenges device design. Other properties – such as thermal conductivity and shaping ability – should also be considered for real-world applications.[48] In this regard, we evaluated the thermal conductivity of $(C_n)_2CuX_4$ (X = Cl, Br, $n$ = even 16–22) by the laser flash method, which showed a thermal conductivity of 0.2 W °C$^{-1}$ m$^{-1}$ (Fig. S15 and S16).[2] The low thermal conductivity agrees with traditional (solid and non-solid) PCMs.[2] However, the hybrid compositions of alkylammonium perovskites may facilitate the tunability of the thermodynamic and transport properties by selectively varying the composition of the two sublattices (*i.e.*, the inorganic and organic layers). Specifically, the inorganic layers of 2D perovskites provide a unique means of tuning essential properties for thermal energy applications, including hysteresis, thermal conductivity, and mechanical strength. Here, concepts and methodologies developed in the field of halide perovskites for light-absorbing and light-emitting applications may be applied.[49–52] To advance toward real applications, we also demonstrate that solvent-free mechanochemical synthesis is feasible for these materials, which is critical for sustainable life-cycle analysis.[53]

# 3. Conclusions

Alkylammonium perovskites exhibit first-order phase transitions with a large latent heat ($>$50 J g$^{-1}$), making them suitable for solid-state thermal management. The new halide perovskites reported here are suitable for medium-temperature applications, which are increasingly sought, especially in improving heat pumping and waste heat recovery in the industrial sector. By synthesizing and characterizing novel $(C_n)_2CuX_4$ (X = Cl, Br; $n$ = even, 16–22), we expand the functional temperature range of this class of materials above 80 °C. Structural and thermodynamic characterization reveals that the polymorphism depends critically on the halide site. We finally show that the low hysteresis (0.1–1 °C) and high d$T$/d$p$ (300 °C GPa$^{-1}$) also render these materials interesting candidates for medium-temperature barocaloric applications. Altogether, our findings should stimulate further exploration of the chemical space for similar compounds for applications above room temperature.

# 4. Experimental section

## 4.1. Materials

**4.1.1. General considerations.** The chemicals used in the different synthesis were adquired from commercial sources:

ethanol (95%, Sigma-Aldrich), diethyl ether (≥99%, Sigma-Aldrich), hydrochloric acid (37%, Sigma-Aldrich), hydrobromic acid (48%, Sigma-Aldrich), copper(II) chloride (99%, Sigma-Aldrich), copper(II) bromide (99%, Sigma-Aldrich), hexadecan-1-amine (98%, Sigma-Aldrich), octadecan-1-amine (97%, Fisher ThermoScientific), nonadecan-1-amine (96%, TCI), icosan-1-amine (95%, BLD pharma), docosan-1-amine (95%, BLD pharma). Octadecane-1-amine, nonadecane-1-amine, icosan-1-amine and docosan-1-amine were stored in the freezer.

**4.1.2. Synthesis of $(CH_3(CH_2)_{15}NH_3)_2CuCl_4$.** Solid $CH_3(CH_2)_{15}NH_2$ (1002 mg, 4.15 mmol) was dissolved in ethanol (96% in water, 10 mL) at 70 °C and HCl aq. (37% in water, 412 μL) was added to the solution. The mixture was cooled to room temperature. The precipitate was filtered, washed with ethanol, and dried under vacuum. Powders of $CH_3(CH_2)_{15}NH_3Cl$ (456 mg, 1.64 mmol) were dissolved in ethanol (96% in water, 4 mL) at 70 °C, and a solution of $CuCl_2$ (883 mg, 6.57 mmol) in ethanol (96% in water, 6 mL) was added. The mixture was heated and stirred until the initial precipitate was dissolved. The solution was left to cool to room temperature. The resulting yellow precipitate was filtered, washed with ethanol, and dried under vacuum for 12 h to yield 299 mg (52.9% yield from the amine salt) of the product. Anal. calc. for $(CH_3(CH_2)_{15}NH_3)_2CuCl_4{\cdot}H_2O$ ($C_{32}H_{74}Cl_4CuN_2O$) C, 54.26%; H, 10.53%; N, 3.96%. Found: C, 54.05%; H, 10.40%; N, 3.96%.

**4.1.3. Synthesis of $(CH_3(CH_2)_{17}NH_3)_2CuCl_4$.** Solid $CH_3(CH_2)_{17}NH_2$ (1118 mg, 4.15 mmol) was dissolved in ethanol (96% in water, 10 mL) at 70 °C and HCl aq. (37% in water, 412 μL) was added to the solution. The mixture was cooled to room temperature. The precipitate was filtered, washed with ethanol, and dried under vacuum. Powders of $CH_3(CH_2)_{17}NH_3Cl$ (304 mg, 0.99 mmol) were dissolved in ethanol (96% in water, 4 mL) at 70 °C, and a solution of $CuCl_2$ (535 mg, 3.9 mmol) in ethanol (96% in water, 6 mL) was added. The mixture was heated and stirred until the initial precipitate was dissolved. The solution was left to cool to room temperature. The resulting yellow precipitate was filtered, washed with ethanol, and dried under vacuum for 12 h to yield 286 mg (77.7% yield from the amine salt) of the product. Anal. calc. for $C_{36}H_{80}Cl_4CuN_2$ C, 57.93%; H, 10.80%; N, 3.75%. Found: C, 57.83%; H, 10.80%; N, 3.67%.

**4.1.4. Synthesis of $(CH_3(CH_2)_{18}NH_3)_2CuCl_4$.** Solid $CH_3(CH_2)_{18}NH_2$ (1176 mg, 4.15 mmol) was dissolved in ethanol (96% in water, 10 mL) at 70 °C and HCl aq. (37% in water, 412 μL) was added to the solution. The mixture was cooled to room temperature. The precipitate was filtered, washed with ethanol, and dried under vacuum. Powders of $CH_3(CH_2)_{18}NH_3Cl$ (230 mg, 0.72 mmol) were dissolved in ethanol (96% in water, 4 mL) at 70 °C, and a solution of $CuCl_2$ (387 mg, 2.88 mmol) in ethanol (96% in water, 6 mL) was added. The mixture was heated and stirred until the initial precipitate was dissolved. The solution was left to cool to room temperature. The resulting yellow precipitate was filtered, washed with ethanol, and dried under vacuum for 12 h to yield 208 mg (75.1% yield from the amine salt) of the product.

**4.1.5. Synthesis of $(CH_3(CH_2)_{19}NH_3)_2CuCl_4$.** Solid $CH_3(CH_2)_{19}NH_2$ (286 mg, 0.96 mmol) was dissolved in ethanol (96% in water, 5 mL) at 70 °C and HCl aq. (37% in water, 95.7 μL) was added to the solution. The mixture was cooled to room temperature. The precipitate was filtered, washed with ethanol, and dried under vacuum. Powders of $CH_3(CH_2)_{19}NH_3Cl$ (59 mg, 0.18 mmol) were dissolved in ethanol (96% in water, 2 mL) at 70 °C, and a solution of $CuCl_2$ (96 mg, 0.71 mmol) in ethanol (96% in water, 3 mL) was added. The mixture was heated and stirred until the initial precipitate was dissolved. The solution was left to cool to room temperature. The resulting yellow precipitate was filtered, washed with ethanol, and dried under vacuum for 12 h to obtain 299 mg (78.8% yield from the amine salt) of the product. Anal. calc. for $(CH_3(CH_2)_{19}NH_3)_2CuCl_4{\cdot}H_2O$ ($C_{40}H_{90}Cl_4CuN_2O$) C, 58.55%; H, 11.06%; N, 3.41%. Found: C, 58.78%; H, 10.93%; N, 3.41%.

**4.1.6. Synthesis of $(CH_3(CH_2)_{21}NH_3)_2CuCl_4$.** Solid $CH_3(CH_2)_{21}NH_2$ (300 mg, 0.92 mmol) was dissolved in ethanol (96% in water, 5 mL) at 70 °C and HCl aq. (37% in water, 91.5 μL) was added to the solution. The mixture was cooled to room temperature. The precipitate was filtered, washed with ethanol, and dried under vacuum. Powders of $CH_3(CH_2)_{21}NH_3Cl$ (149 mg, 0.41 mmol) were dissolved in ethanol (96% in water, 2 mL) at 70 °C, and a solution of $CuCl_2$ (221 mg, 1.65 mmol) in ethanol (96% in water, 5 mL) was added. The mixture was heated and stirred until the initial precipitate was dissolved. The solution was left to cool to room temperature. The resulting yellow precipitate was filtered, washed with ethanol, and dried under vacuum for 12 h to yield 145 mg (82.2% yield from the amine salt) of the product. Anal. calc. for $C_{44}H_{96}Cl_4CuN_2$ C, 61.55%; H, 11.27%; N, 3.26%. Found: C, 61.49%; H, 11.28%; N, 3.24%.

**4.1.7. Synthesis of $(CH_3(CH_2)_{15}NH_3)_2CuBr_4$.** Solid $CH_3(CH_2)_{15}NH_2$ (1000 mg, 4.14 mmol) was dissolved in ethanol (96% in water, 10 mL) at 70 °C and HBr aq. (48% in water, 566 μL) was added to the solution. The mixture was cooled to room temperature. The precipitate was filtered, washed with ethanol, and dried under vacuum. Powders of $CH_3(CH_2)_{15}NH_3Br$ (300 mg, 0.93 mmol) were mixed with $CuBr_2$ (104 mg, 0.47 mmol) and dissolved in ethanol (96% in water, 2.42 mL). The mixture was stirred and heated to 80 °C until the reagents were dissolved. The solution was cooled to 40 °C. The resulting dark purple precipitate was filtered, washed with diethyl ether, and dried under vacuum for 12 h to yield 168 mg (40.7% yield from the amine salt) of the product. Anal. calc. for $C_{32}H_{72}Br_4CuN_2$ C, 44.27%; H, 8.36%; N, 3.23%. Found: C, 44.23%; H, 8.34%; N, 3.17%.

**4.1.8. Synthesis of $(CH_3(CH_2)_{15}NH_3)_2CuBr_4$ by mechanochemistry.** Powders of $CH_3(CH_2)_{15}NH_3Br$ (300 mg, 0.93 mmol) were mixed with $CuBr_2$ (104 mg, 0.47 mmol) and two $ZrO_2$ balls of 3 mm in diameter into a 2-mL polypropylene Eppendorf vial. The purple powder was separated after milling at 30 Hz for 1.5 h in a Retsch MM400 miller.

**4.1.9. Synthesis of $(CH_3(CH_2)_{17}NH_3)_2CuBr_4$.** Solid $CH_3(CH_2)_{17}NH_2$ (1000 mg, 3.71 mmol) was dissolved in ethanol (96% in water, 10 mL) at 70 °C and HBr aq. (48% in water, 507 μL) was added to the solution. The mixture was cooled to room temperature. The precipitate was filtered, washed with ethanol, and dried under vacuum. Powders of $CH_3(CH_2)_{17}NH_3Br$ (300 mg, 0.86 mmol) were mixed with $CuBr_2$ (97 mg, 0.43 mmol) and

dissolved in ethanol (96% in water, 2.37 mL). The mixture was stirred and heated to 80 °C until the reagents were dissolved. The solution was cooled to 40 °C. The resulting dark purple precipitate was filtered, washed with diethyl ether, and dried under vacuum for 12 h to obtain 199 mg of product (50.5% yield from amine salt). Anal. calc. for $C_{36}H_{80}Br_4CuN_2$ C, 46.79%; H, 8.73%; N, 3.03%. Found: C, 46.79%; H, 8.70%; N, 3.01%.

**4.1.10. Synthesis of $(CH_3(CH_2)_{18}NH_3)_2CuBr_4$.** Solid $CH_3(CH_2)_{18}NH_2$ (1000 mg, 3.52 mmol) was dissolved in ethanol (96% in water, 10 mL) at 70 °C and HBr aq. (48% in water, 482 μL) was added to the solution. The mixture was cooled to room temperature. The precipitate was filtered, washed with ethanol, and dried under vacuum. Powders of $CH_3(CH_2)_{18}NH_3Br$ (300 mg, 0.82 mmol) were mixed with $CuBr_2$ (92 mg, 0.41 mmol) and dissolved in ethanol (96% in water, 2.35 mL). The mixture was stirred and heated to 80 °C until the reagents were completely dissolved. The solution was cooled to 60 °C. The resulting dark purple precipitate was filtered, washed with diethyl ether, and dried under vacuum for 12 h to obtain 181 mg (46.2% yield from amine salt) of the product.

**4.1.11. Synthesis of $(CH_3(CH_2)_{19}NH_3)_2CuBr_4$.** Solid $CH_3(CH_2)_{19}NH_2$ (1000 mg, 3.36 mmol) was dissolved in ethanol (96% in water, 10 mL) at 70 °C and HBr aq. (48% in water, 459 μL) was added to the solution. The mixture was cooled to room temperature. The precipitate was filtered, washed with ethanol, and dried under vacuum. Powders of $CH_3(CH_2)_{19}NH_3Br$ (300 mg, 0.79 mmol) were mixed with $CuBr_2$ (88 mg, 0.39 mmol) and dissolved in ethanol (96% in water, 2.35 mL). The mixture was stirred and heated at 80 °C until the reagents were dissolved. The solution was cooled to 60 °C. The resulting dark purple precipitate was filtered, washed with diethyl ether, and dried under vacuum for 12 h to obtain 167 mg (42.9% yield from the amine salt) of the product. Anal. calc. for $C_{40}H_{88}Br_4N_2Cu$ C, 49.01%; H, 9.05%; N, 2.86%. Found: C, 49.19%; H, 9.12%; N, 2.84%.

**4.1.12. Synthesis of $(CH_3(CH_2)_{21}NH_3)_2CuBr_4$.** Solid $CH_3(CH_2)_{21}NH_2$ (1000 mg, 3.07 mmol) was dissolved in ethanol (96% in water, 10 mL) at 70 °C and HBr aq. (48% in water, 420 μL) was added to the solution. The mixture was cooled to room temperature. The precipitate was filtered, washed with ethanol, and dried under vacuum. Powders of $CH_3(CH_2)_{21}NH_3Br$ (300 mg, 0.74 mmol) were mixed with $CuBr_2$ (82 mg, 0.37 mmol) and dissolved in ethanol (96% in water, 2.29 mL). The mixture was stirred and heated to 80 °C until the reagents were completely dissolved. The solution was cooled to 60 °C. The resulting purple precipitate was filtered, washed with diethyl ether, and dried under vacuum for 12 hours to obtain 136 mg (35.5% yield from amine salt). Anal. calc. for $(CH_3(CH_2)_{21}NH_3)_2CuBr_4{\cdot}3H_2O$ ($C_{44}H_{102}Br_4CuN_2O_3$) C, 48.46%; H, 9.43%; N, 2.57%. Found: C, 48.87%; H, 9.02%; N, 2.56%.

### 4.2. Methods

**4.2.1. Single-crystal X-ray diffraction.** Single-crystal X-ray diffraction (SCXRD) data for $(CH_3(CH_2)_{15}NH_3)_2CuCl_4$ and $(CH_3(CH_2)_{17}NH_3)_2CuCl_4$ were collected in a Bruker D8 Venture at the research facilities of the Universitat de Barcelona (CCiTUB) at MoKα ($\lambda$ = 0.71073 Å). Data for $(CH_3(CH_2)_{15}NH_3)_2CuBr_4$ and $(CH_3(CH_2)_{21}NH_3)_2CuBr_4$ were collected at the BL13-XALOC beamline (ALBA, Barcelona, Spain) at $\lambda$ = 0.72932 Å. The crystals were mounted with Paratone N grease on a loop and placed in the $N_2$ stream of an Oxford Cryosystem. Frames were collected, and unit-cell parameters were refined against all data. Space-group assignments were based upon systematic absences, E-statistics, agreement factors for equivalent reflections, and successful refinement of the structures. Structures were solved using the intrinsic phasing method implemented in SHELXT-2014.[54] Solutions were refined against all data using SHELXL-2018/34[55] and OLEX.[56] The refining includes anisotropic displacement parameters except for the hydrogen atoms, which were calculated. Details regarding data quality and a summary of the residual values of the refinements are listed in Tables S1–S4.

We used the Mercury software to estimate the angles between the alkylammonium cations and the plane formed by the Cu–X octahedra (X = Cl, Br). We drew a plane consisting of the carbon atoms in anti-conformation of the alkylammonium cations. We calculated the angle between this plane and the (002) plane, which is formed by Cu–X octahedra. No remarkable difference was observed if odd or even carbons were used (being C1 the adjacent carbon to the ammonium atom). We averaged the angles formed between the independent alkylammonium cations and the (002) plane, and estimated the error *via* standard deviation. The largest error was used for all the angles (1°).

**4.2.2. Powder X-ray diffraction.** Powder X-Ray diffraction (PXRD) measurements were performed at the Universitat de Barcelona research facilities (CCiTUB). We used a PANalytical X'Pert PRO MPD θ/θ powder diffractometer of 240 millimeters of radius, in a configuration of convergent beam with a focusing mirror and a transmission geometry with flat samples sandwiched between low-absorbing films. The Cu Kα radiation ($\lambda$ = 1.5418 Å) was set at 45 kV and 40 mA. Incident beam slits were defined to have a beam height of 0.4 millimeters. We measured with a step size of 0.0263° and a measuring time of 300 seconds per step. To avoid preferential orientation of the samples, powders of each 2D perovskite were added into a 2-mL polypropylene Eppendorf vial and ball-milled using 3-mm-diameter $ZrO_2$ balls in a Retsch MM400 miller for 10 minutes at 30 Hz. The samples were sandwiched between films of polyester mylar of 3.6 microns in thickness.

**4.2.3. Elemental analysis.** Elemental analysis was performed on an EA3100 Microanalitzador Elemental (Thermo-Scientific) in NCH configuration using the dynamic flash combustion method and helium as a carrier gas.

**4.2.4. Differential scanning calorimetry.** Differential scanning calorimetry (DSC) was conducted at various scanning rates (1–20 K $min^{-1}$) and for several cycles on the synthesized samples using a DSCQ100 (TA Instruments) by encapsulating 5–10 mg of each sample inside hermetically sealed aluminum pans and placing them under a $N_2$ atmosphere. Latent heat and temperature calibrations were done using the melting of indium. Latent heats were obtained by integration of the heat flow after baseline correction. Temperature-dependent heat flow $dQ/|dT|$ was obtained as $dQ/|dT| = \dot{Q}/\dot{T}$.

Heat capacity was measured for ~5 mg of $(C_{16})_2CuBr_4$. Experiments were conducted on a commercial DSC250 (TA instruments) operating in modulated mode, with an amplitude of 1 °C, a period of 120 s, and a temperature rate of 2 °C $min^{-1}$.

**4.2.5. High-pressure differential thermal analysis.** High-pressure differential thermal analysis (HP-DTA) measurements were performed using a homemade calorimeter, consisting of a high-pressure cell operating up to 250 MPa and from room temperature to 200 °C. Heating rates at 3 °C $min^{-1}$ were controlled using a resistive heater, and cooling runs were achieved through an air stream. Samples were encapsulated inside tin capsules in powder form mixed with silicon oil Therm-240 (Lauda). A closed hole was drilled in the tin capsules to insert Bridgman thermocouples, which acted as thermal sensors. The external pressure transmitting medium outside the capsule and inside the pressure circuit was also Therm-240 (Lauda).

**4.2.6. Thermal gravimetric analysis.** Thermal gravimetric analysis (TGA) was performed using a Q50 system from TA Instruments under $N_2$ atmosphere from room temperature to 450–550 °C at a heating rate of 5 °C $min^{-1}$. A sample mass of ~5 mg was used.

**4.2.7. Thermal diffusivity measurements.** Thermal diffusivity was measured with the laser flash method (Netzsch LFA 457 MicroFlash). A powder pellet of $(C_{16})_2CuBr_4$ was fabricated by applying 4 tons for 30 seconds, obtaining a 178.9 mg cylinder of 0.981 mm thick and 12.98 mm in diameter, leading to a relative density of 89.3%. The resulting signals were fitted with the software Proteus 7.1, using the standard Cape-Lehman model[57] with a linear baseline and an additional correction for radiative transfer inside the transparent pellets.[58]

## Author contributions

A. P., L. R.-C., C. P.-J., G. C., and M. B. performed the materials synthesis and characterization; R. M., X. C., and R. B. performed the single-crystal X-ray diffraction experiments; G. N. and F. G. performed the thermal conductivity experiments; all authors discussed the results and edited the manuscript; R. M., P. L., and J.-L. T. conceptualized the research and raised research funds; R. M. and P. L. supervised the project and wrote the first draft.

## Conflicts of interest

There are no conflicts of interest to declare.

## Data availability

Data supporting this article have been included as part of the supplementary information (SI). Supplementary information: crystallographic tables, powder X-ray diffraction patterns, and thermodynamic measurements at normal and high pressure. See DOI: **https://doi.org/10.1039/d5qm00712g**.

CCDC 2451955–2451958 contain the supplementary crystallographic data for this paper.[59a–d]

## Acknowledgements

This work has been funded by the EIC Pathfinder Challenge 2022 of the Horizon Europe Program under grant agreement 101114987, financed by the European Union. The authors are grateful for access to the ALBA Synchrotron at XALOC beamline for beamtime under proposal 2024018033. R. M. acknowledges support from Ministerio de Ciencia, Innovación y Universidades and Agencia Estatal de Investigación (RYC2021-031578-I, PID2022-137777NA-I00, CEX2021-001202-M) funded by MICIU and by ERDF/EU. This work was also supported by SGR-00343 Project (Catalonia), by Grant PID2023-146623NB-I00 funded by MICIU and by ERDF/EU, and is part of the Maria de Maeztu Units of Excellence Programme CEX2023-001300-M/funded by MCIN/AEI/10.13039/501100011033.

## References

1 A. Usman, F. Xiong, W. Aftab, M. Qin and R. Zou, Emerging Solid-to-Solid Phase-Change Materials for Thermal-Energy Harvesting, Storage, and Utilization, *Adv. Mater.*, 2022, **34**, 2202457.
2 Ž. Ahčin, A. Kitanovski and J. Tušek, Latent thermal energy storage using solid-state phase transformation in caloric materials, *Cell Rep. Phys. Sci.*, 2025, **5**(9), 102175.
3 K. Matuszek, M. Kar, J. M. Pringle and D. R. MacFarlane, Phase Change Materials for Renewable Energy Storage at Intermediate Temperatures, *Chem. Rev.*, 2023, **123**, 491–514.
4 H. Jouhara, N. Khordehgah, S. Almahmoud, B. Delpech, A. Chauhan and S. A. Tassou, Waste heat recovery technologies and applications, *Therm. Sci. Eng. Prog.*, 2018, **6**, 268–289.
5 N. I. Md, G. Maruf, J. Morales-España, N. Sijm, N. Helistö and J. Kiviluoma, Classification, potential role, and modeling of power-to-heat and thermal energy storage in energy systems: A review, *Sustainable Energy Technol. Assess.*, 2022, **53**, 102553.
6 X. Moya and N. D. Mathur, Caloric materials for cooling and heating, *Science*, 2020, **370**, 797–803.
7 A. Jamekhorshid, S. M. Sadrameli and M. Farid, A review of microencapsulation methods of phase change materials (PCMs) as a thermal energy storage (TES) medium, *Renewable Sustainable Energy Rev.*, 2014, **31**, 531–542.
8 M. Barrio, J. Font, D. O. López, J. Muntasell and J. Ll, Tamarit, Floor radiant system with heat storage by a solid-solid phase transition material, *Sol. Energy Mater. Sol. Cells*, 1992, **27**, 127–133.
9 A. Serrano, J.-L. Dauvergne, S. Doppiu and E. Palomo Del Barrio, Neopentyl Glycol as Active Supporting Media in Shape-Stabilized PCMs, *Materials*, 2019, **12**, 3169.

10 V. Busico, C. Carfagna, V. Salerno, M. Vacatello and F. Fittipaldi, The layer perovskites as thermal energy storage systems, *Sol. Energy*, 1980, **24**, 575–579.
11 M. Vacatello, M. de Girolamo and V. Busico, Relationships between structure and properties in long-chain bis(n-alkylammonium)tetrabromocuprates(II) and bis(n-alkylammonium)tetrabromomanganates(II), *J. Chem. Soc., Faraday Trans. 1*, 1981, **77**, 2367–2375.
12 M. Vacatello, Relation between the properties and structure of compounds of the type bis(alkylammonium) tetrachlorocuprate, *Ann. Chim. Rome Italy*, 1974, **64**, 19–25.
13 M. Vacatello, Solid-solid phase transitions in compounds of the type bis(alkylammonium)tetrachlorocuprate, *Ann. Chim. Rome Italy*, 1974, **64**, 13–18.
14 J. Li, M. Barrio, D. J. Dunstan, R. Dixey, X. Lou, J.-L. Tamarit, A. E. Phillips and P. Lloveras, Colossal Reversible Barocaloric Effects in Layered Hybrid Perovskite $(C_{10}H_{21}NH_3)_2$-$MnCl_4$ under Low Pressure Near Room Temperature, *Adv. Funct. Mater.*, 2021, **31**, 2105154.
15 R. L. Kingsford, S. R. Jackson, L. C. Bloxham and C. G. Bischak, Controlling Phase Transitions in Two-Dimensional Perovskites through Organic Cation Alloying, *J. Am. Chem. Soc.*, 2023, **145**, 11773–11780.
16 M. D. Smith, E. J. Crace, A. Jaffe and H. I. Karunadasa, The Diversity of Layered Halide Perovskites, *Annu. Rev. Mater. Res.*, 2018, **48**, 111–136.
17 D. Solis-Ibarra, I. C. Smith and H. I. Karunadasa, Post-synthetic halide conversion and selective halogen capture in hybrid perovskites, *Chem. Sci.*, 2015, **6**, 4054–4059.
18 D. B. Mitzi, *Prog. Inorg. Chem.*, 1999, 1–121.
19 W. Li, Z. Wang, F. Deschler, S. Gao, R. H. Friend and A. K. Cheetham, Chemically diverse and multifunctional hybrid organic–inorganic perovskites, *Nat. Rev. Mater.*, 2017, **2**, 16099.
20 E. J. Dalley, L. C. Bloxham, J. R. Muralidhar, P. W. Martin, I. J. Kim and C. G. Bischak, Chain-Melting Temperature Depression in the Organic Layer of Two-Dimensional Perovskites, *ACS Energy Lett.*, 2024, **9**, 5756–5762.
21 M. Kumar and S. Vasudevan, Alkyl Chain Alloying and the Optical Band Gap of the Layered Lead Halide Perovskites: The Role of Interlayer Chain–Chain Interactions, *J. Phys. Chem. C*, 2025, **129**, 5122–5132.
22 R. Salgado-Pizarro, C. Barreneche and A. I. Fernández, Synthesis optimisation of copper-based layered perovskites as thermal energy storage materials, *Mater. Today Chem.*, 2023, **30**, 101491.
23 Y. Gao, H. Liu, F. Hu, H. Song, H. Zhang, J. Hao, X. Liu, Z. Yu, F. Shen, Y. Wang, H. Zhou, B. Wang, Z. Tian, Y. Lin, C. Zhang, Z. Yin, J. Wang, Y. Chen, Y. Li, Y. Song, Y. Shi, T. Zhao, J. Sun, Q. Huang and B. Shen, Reversible colossal barocaloric effect dominated by disordering of organic chains in $(CH_3–(CH_2)_{n-1}–NH_3)_2MnCl_4$ single crystals, *NPG Asia Mater.*, 2022, **14**, 34.
24 P. K. Mukherjee, Phase transitions among the rotator phases of the normal alkanes: A review, *Phys. Rep.*, 2015, **588**, 1–54.
25 R. Matheu, J. A. Vigil, E. J. Crace and H. I. Karunadasa, The halogen chemistry of halide perovskites, *Trends Chem.*, 2022, **4**, 206–219.
26 P.-H. Denis, M. Mertens, W. T. M. Van Gompel, K. Van Hecke, B. Ruttens, J. D'Haen, L. Lutsen and D. Vanderzande, Directing the Self-Assembly of Conjugated Organic Ammonium Cations in Low-Dimensional Perovskites by Halide Substitution, *Chem. Mater.*, 2021, **33**, 5177–5188.
27 J. Seo, R. Ukani, J. Zheng, J. D. Braun, S. Wang, F. E. Chen, H. K. Kim, S. Zhang, C. Thai, R. D. McGillicuddy, H. Yan, J. J. Vlassak and J. A. Mason, Barocaloric Effects in Dialkylammonium Halide Salts, *J. Am. Chem. Soc.*, 2024, **146**, 2736–2747.
28 N. Hoshino, S. Tamura and T. Akutagawa, Negative-to-Positive Thermal Conductivity Temperature Coefficient Transition Induced by Dynamic Fluctuations of the Alkyl Chains in the Layered Complex $(C_4H_9NH_3)_2CuCl_4$, *Chem. – Eur. J.*, 2020, **26**, 2610–2618.
29 D. Lu, Y. Di and J. Dou, Crystal structures and solid–solid phase transitions on phase change materials $(C_nH_{2n+1}$-$NH_3)_2CuCl_4$(s) ($n$ = 10 and 11), *Sol. Energy Mater. Sol. Cells*, 2013, **114**, 1–8.
30 D.-H. He, Y.-Y. Di, Y. Yao, Y.-P. Liu and W.-Y. Dan, Crystal Structure, Low-Temperature Heat Capacities, and Thermodynamic Properties of Bis(dodecylammonium) Tetrachlorocuprate $(C_{12}H_{28}N)_2CuCl_4$(s), *J. Chem. Eng. Data*, 2010, **55**, 5739–5744.
31 D.-H. He, Y.-Y. Di, Z.-C. Tan, F.-F. Yi, W.-Y. Dan and Y.-P. Liu, Crystal structures and thermochemistry on phase change materials $(n\text{-}C_nH_{2n+1}NH_3)_2CuCl_4$(s) (n = 14 and 15), *Sol. Energy Mater. Sol. Cells*, 2011, **95**, 2897–2906.
32 J. Seo, R. D. McGillicuddy, A. H. Slavney, S. Zhang, R. Ukani, A. A. Yakovenko, S.-L. Zheng and J. A. Mason, Colossal barocaloric effects with ultralow hysteresis in two-dimensional metal–halide perovskites, *Nat. Commun.*, 2022, **13**, 2536.
33 R. F. I. Josey and J. L. Fenton, Variable Mechanical Properties in Layered Copper Bromide Hybrid Solids Based on Configuration of Organic Cations, *Inorg. Chem.*, 2024, **63**, 6026–6032.
34 F. Palazon, Y. El Ajjouri and H. J. Bolink, Making by Grinding: Mechanochemistry Boosts the Development of Halide Perovskites and Other Multinary Metal Halides, *Adv. Energy Mater.*, 2020, **10**, 1902499.
35 R. Kind, S. Plesko, H. Arend, R. Blinc, B. Zeks, J. Seliger, B. Lozar, J. Slak, A. Levstik, C. Filipic, V. Zagar, G. Lahajnar, F. Milia and G. Chapuis, Dynamics of the n-decylammonium chains in the perovskite-type layer structure compound $(C_{10}H_{21}NH_3)_2CdCl_4$, *J. Chem. Phys.*, 1979, **71**, 2118–2130.
36 R. Salgado-Pizarro, A. Svobodova-Sedlackova, A. I. Fernández and C. Barreneche, Designing thermal regulation materials: Investigating alkylamine length in polymorphic layered hybrid organic-inorganic perovskites, *J. Energy Storage*, 2023, **73**, 109156.
37 A. Aznar, P. Lloveras, M. Barrio, P. Negrier, A. Planes, L. Mañosa, N. D. Mathur, X. Moya and J.-L. Tamarit, Reversible and irreversible colossal barocaloric effects in plastic crystals, *J. Mater. Chem. A*, 2020, **8**, 639–647.

38 F. Guillou, F. Wilhelm, O. Tegus and A. Rogalev, Microscopic mechanism of the giant magnetocaloric effect in MnCoGe alloys probed by x-ray magnetic circular dichroism, *Appl. Phys. Lett.*, 2016, **108**, 122405.

39 Y.-Y. Zhao, F.-X. Hu, L.-F. Bao, J. Wang, H. Wu, Q.-Z. Huang, R.-R. Wu, Y. Liu, F.-R. Shen, H. Kuang, M. Zhang, W.-L. Zuo, X.-Q. Zheng, J.-R. Sun and B.-G. Shen, Giant Negative Thermal Expansion in Bonded MnCoGe-Based Compounds with $Ni_2In$-Type Hexagonal Structure, *J. Am. Chem. Soc.*, 2015, **137**, 1746–1749.

40 Q. Y. Ren, W. D. Hutchison, J. L. Wang, A. J. Studer and S. J. Campbell, First-order magneto-structural transition and magnetocaloric effect in $Mn(Co_{0.96}Fe_{0.04})Ge$, *J. Alloys Compd.*, 2017, **693**, 32–39.

41 T. Samanta, D. L. Lepkowski, A. U. Saleheen, A. Shankar, J. Prestigiacomo, I. Dubenko, A. Quetz, I. W. H. Oswald, G. T. McCandless, J. Y. Chan, P. W. Adams, D. P. Young, N. Ali and S. Stadler, Hydrostatic pressure-induced modifications of structural transitions lead to large enhancements of magnetocaloric effects in MnNiSi-based systems, *Phys. Rev. B*, 2015, **91**, 020401.

42 R.-R. Wu, L.-F. Bao, F.-X. Hu, H. Wu, Q.-Z. Huang, J. Wang, X.-L. Dong, G.-N. Li, J.-R. Sun, F.-R. Shen, T.-Y. Zhao, X.-Q. Zheng, L.-C. Wang, Y. Liu, W.-L. Zuo, Y.-Y. Zhao, M. Zhang, X.-C. Wang, C.-Q. Jin, G.-H. Rao, X.-F. Han and B.-G. Shen, Giant barocaloric effect in hexagonal $Ni_2In$-type Mn-Co-Ge-In compounds around room temperature, *Sci. Rep.*, 2015, **5**, 18027.

43 A. Salvatori, P. Negrier, A. Aznar, M. Barrio, J. L. Tamarit and P. Lloveras, Colossal barocaloric effects in adamantane derivatives for thermal management, *APL Mater.*, 2022, **10**, 111117.

44 Z. Zhang, K. Li, S. Lin, R. Song, D. Yu, Y. Wang, J. Wang, S. Kawaguchi, Z. Zhang, C. Yu, X. Li, J. Chen, L. He, R. Mole, B. Yuan, Q. Ren, K. Qian, Z. Cai, J. Yu, M. Wang, C. Zhao, X. Tong, Z. Zhang and B. Li, Thermal batteries based on inverse barocaloric effects, *Sci. Adv.*, 2023, **9**, eadd0374.

45 J. C. S. Costa, A. Mendes and L. M. N. B. F. Santos, Chain Length Dependence of the Thermodynamic Properties of n-Alkanes and their Monosubstituted Derivatives, *J. Chem. Eng. Data*, 2018, **63**, 1–20.

46 S. Wang, M. Mandal, H. Zhang, D. W. Breiby, O. Yildiz, Z. Ling, G. Floudas, M. Bonn, D. Andrienko, H. I. Wang, P. W. M. Blom, W. Pisula and T. Marszalek, Odd–Even Alkyl Chain Effects on the Structure and Charge Carrier Transport of Two-Dimensional Sn-Based Perovskite Semiconductors, *J. Am. Chem. Soc.*, 2024, **146**, 19128–19136.

47 N. Zhang, Y. Song, Y. Du, Y. Yuan, G. Xiao and Y. Gui, A Novel Solid–Solid Phase Change Material: Pentaglycerine/Expanded Graphite Composite PCMs, *Adv. Eng. Mater.*, 2018, **20**, 1800237.

48 A. Serrano, I. Garrido, S. Santos, M. Duran, J.-L. Dauvergne, M. Carmona and E. Palomo Del Barrio, Effect of processing on microstructure and mechanical properties of pentaglycerine based solid-solid phase change materials, *J. Energy Storage*, 2022, **55**, 105677.

49 C. R. Deschene, C. Zwanziger, R. Matheu and H. I. Karunadasa, Mixed-valence halide perovskites, *Coord. Chem. Rev.*, 2025, **539**, 216719.

50 H. Dong, C. Ran, W. Gao, M. Li, Y. Xia and W. Huang, Metal Halide Perovskite for next-generation optoelectronics: progresses and prospects, *eLight*, 2023, **3**, 3.

51 A. Kojima, K. Teshima, Y. Shirai and T. Miyasaka, Organometal Halide Perovskites as Visible-Light Sensitizers for Photovoltaic Cells, *J. Am. Chem. Soc.*, 2009, **131**, 6050–6051.

52 L. Protesescu, S. Yakunin, M. I. Bodnarchuk, F. Krieg, R. Caputo, C. H. Hendon, R. X. Yang, A. Walsh and M. V. Kovalenko, Nanocrystals of Cesium Lead Halide Perovskites ($CsPbX_3$, X = Cl, Br, and I): Novel Optoelectronic Materials Showing Bright Emission with Wide Color Gamut, *Nano Lett.*, 2015, **15**, 3692–3696.

53 J.-A. Alberola-Borràs, R. Vidal and I. Mora-Seró, Evaluation of multiple cation/anion perovskite solar cells through life cycle assessment, *Sustain, Energy Fuels*, 2018, **2**, 1600–1609.

54 G. M. Sheldrick, SHELXT – Integrated space-group and crystal-structure determination, *Acta Crystallogr., Sect. A:Found. Adv.*, 2015, **71**, 3–8.

55 G. Sheldrick, *Acta Crystallogr., Sect. A:Found. Crystallogr.*, 2008, **64**, 112–122.

56 O. V. Dolomanov, L. J. Bourhis, R. J. Gildea, J. A. K. Howard and H. Puschmann, OLEX2: a complete structure solution, refinement and analysis program, *J. Appl. Crystallogr.*, 2009, **42**, 339–341.

57 J. A. Cape and G. W. Lehman, Temperature and Finite Pulse-Time Effects in the Flash Method for Measuring Thermal Diffusivity, *J. Appl. Phys.*, 1963, **34**, 1909–1913.

58 R. L. McMasters, J. V. Beck, R. B. Dinwiddie and H. Wang, Accounting for penetration of laser heating in flash thermal diffusivity experiments, *J. Heat Transfer*, 1999, **121**, 15–21.

59 (*a*) CCDC 2451955: Experimental Crystal Structure Determination, 2025, DOI: **10.5517/ccdc.csd.cc2n9gbs**; (*b*) CCDC 2451956: Experimental Crystal Structure Determination, 2025, DOI: **10.5517/ccdc.csd.cc2n9gct**; (*c*) CCDC 2451957: Experimental Crystal Structure Determination, 2025, DOI: **10.5517/ccdc.csd.cc2n9gdv**; (*d*) CCDC 2451958: Experimental Crystal Structure Determination, 2025, DOI: **10.5517/ccdc.csd.cc2n9gfw**.